Article

Design and demonstration of compact, high bandwidth optical mode selective devices by realizing ITO-based controllable phase shifters integrated on silicon-on-insulator waveguides

Hai Ta Duy [1], Duy Nguyen Thi Hang [1], Thuy Tran Thi Thanh [1], Duy Duong Quang [1], Hoang Chu Duc [2], and Cao Dung Truong [1,*]

[1] Posts and Telecommunications Institute of Technology of Vietnam;
[2] Ministry of Science and Technology of Vietnam;
* Correspondence: dungtc@ptit.edu.vn;

Abstract: Recently, Indium Tin Oxide, a highly transparent, well conductive, and CMOS-compatible material, has been paying strong attention to the thermo-optic controlled silicon photonics industry because it allows a miniature of the gap between the core silicon and the heater, thus enabling reducing the electric power consumption and enhancing the switching speed. In this article, we propose an ultralow loss and small-size ITO microheater for the phase shift tuning. The designated microheater is manipulated in realizing a numerical co-design of compact and high bandwidth three-mode converter and three-mode selective router. Simulation results illustrate the 3-dB bandwidth for the three-mode converter and three-mode selective router as much as 100-nm and 40-nm during crosstalk under -25 dB, respectively. Besides, co-designed devices attain relatively large fabrication tolerances corresponding to width and height tolerances of ±50 nm and ±5 nm. In addition, the proposed devices consumed less than 90 mW total power consumption and took a fast switching time below 8 μs. Moreover, both two co-designs can be integrated into an estimated compact footprint of 8 μm×2160 μm. Such excellent performances demonstrate the attractive potential of ITO as low-loss thermo-optic phase shifters and open an alternative way for enabling ultrafast and high-speed mode division multiplexing systems and very large-scale photonic integrated circuits.

Keywords: co-design; ITO; thermo-optic phase shifter; mode selective converter; mode selective router; numerical simulation

1. Introduction

Recently, to respond to rapidly growing demands of transmission capacities in optical networks, mode division multiplexing (MDM) has emerged as a promising solution to enhance the information transmission capacity and processing proficiency to overcome the Shannon limit [1–4]. It is widely considered that, in many technological platforms used to develop microchips components for the optical signal processing issue in general and mode division multiplexing technique in particular for optical communication networks, photonic integrated circuit (PIC) is one of the most preferred technological platforms. PICs have become prevailed technology because PIC can integrate various signal processing components in compact and flexible configurations. Nowadays, silicon-on-insulator (SOI) waveguide-based structures are prevalent for the realization of dense photonic integrated circuits and firmly established within the optoelectronic industry because they contain many advantages of low optical losses over the third telecom wavelength range, high confinement of light in small cross-section, reasonable manufacturing cost thanks to full compatibility with complementary metal-oxide-semiconductor technology [5].

Among essential components for optical mode processing, except for mode multiplexers/demultiplexers [6], [7], most of the mode signal processing components are related to the switching mechanism, such as mode converters [8], mode switches [9–11], mode routers . The switching function of optical signals in silicon photonic waveguides depends on the ability to control the phase of the optical field. The most common way to induce a dynamic phase shift is by exploiting the thermo-optic (TO) coefficient of the silicon core layer because of the sizeable thermo-optic coefficient ($\sim 1.8\times10^{-4}\ K^{-1}$) [12] or exploiting the carrier effect by doping the conductor concentrations of group III/V elements [13], [14]. Although the carrier effect is capable of producing high-speed phase shifts and small size integration, it suffers some drawbacks from the large optical loss and a relatively complex multi-layer fabrication process, thus leading to an expensive cost. In contrast, the phase shift based on the thermo-optic effect can be attained by heating the waveguide with a metallic microheater. This mechanism could be fabricated using the uncomplicated CMOS processes, which still respond to the short switching time in several microseconds. Furthermore, this mechanism can permit ignorable optical losses by locating the lossy microheater at a reliable distance from the waveguide. Nevertheless, such a heater is usually placed far from the core waveguide, which could lead to low-performance on aspects of high power consumption or low switching speeds. Thermo-optic phase shifters are applied in a wide range of current and new integrated photonic applications such as phased arrays [15–17] beam steering [18], reconfigurable photonics [19–21] integrated quantum photonics [22], [23] and neural networks [24], [25]. Especially, thermo-optic phase shifters are indispensable elements in silicon photonic devices since optical phase manipulations are essential to divide or recombine optical patterns. However, for TO devices based on metallic microheaters [26–29] the influence of the upper-cladding material showing a trade-off between the power consumption and the switching speed [30]. Hence, an acceptable way to improve electrical performance is to reduce the gap between the core waveguide and the microheater. Several 2D materials, for example, graphene as a transparent heater, have been chosen to reduce the gap [31], [32]. However, graphene has a relation to complex fabrication processes that have not been yet prepared for massive manufacture. In such a scenario, transparent conducting oxides (TCOs) have been considerably interested in active photonic devices due to their high transparency, good conductivity, and excellent adhesion to substrates. Among the existing TCOs, Indium Tin Oxide (ITO) is being expected as a promising potential to achieve a plethora of efficient electro-optic active devices [33–36]. Because, when electrically tuned, ITO films can deliver unity-strong index modulation [18], [37], incredibly close to its epsilon-near-zero (ENZ) regime in the near-infrared spectrum [38], [39], which leads to inter alia to significant optical nonlinearities [40], [41], and slow-light effects [42]. In the field of silicon photonics, this uniquely specific feature has been utilized to construct high-performance devices since optical losses are significantly reduced in the ENZ regime. One of the significant interests surrounding ITO is to realize its applied potential as controllable and ultra-low loss phase shifters for wide silicon photonic active devices [43], [44].

In MDM systems, multimode converter (MMC) [45], and multimode selective router (MSR) [10] are vital elements for realizing a flexible mode processing system. In this paper, we propose and design transparent ITO heaters for high-performance TO tuning of silicon photonic structures based on numerical simulation processes. The ultra-low loss ITO heater is utilized to realize compact and high bandwidth mode selective devices with significant performances of low-loss, ultra-low crosstalk, large fabrication tolerance, low power consumption, and short switching time. The spacing influence between the core waveguide and the ITO microheater and the geometrical optimizations of silicon photonic devices based on ITO phase shifters are investigated and characterized for TE polarization.

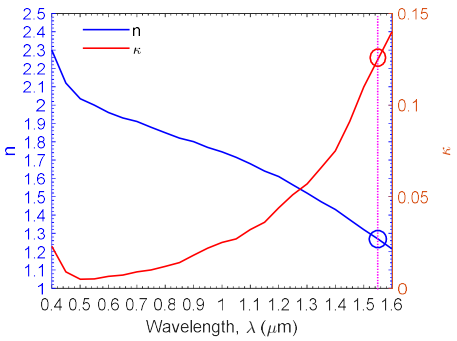

Fig.1. Spectral behavior of real (blue) and imaginary (red) parts of the refractive index of sputtered films by using different oxygen flow-rate and the post-deposition heat treatment process.

2. Materials and Methods

Current photonic integrated circuits mainly utilize phase modulation to control the light signals. One of the most popular phase modulation methods is to change the refractive index, n, and Kramers-Kronig (K-K) relations through electro-optic, thermo-optic, or carrier effects. Optical performances of a photonic integrated device strongly depend on lower physical mechanisms, especially to carrier effect relating to optical loss due to conductive absorption caused by doped particle population. ITO material can be used as an electro-optic (EO) case in the n–dominant regime or for the electro-absorptive (EA) cases in the κ–dominant regime depending on the biased carrier condition and relative position to the epsilon-near-zero (ENZ) point. The optical property of ITO ($\varepsilon = \varepsilon' + j\varepsilon''$) in the telecom window of the near infrared spectrum can be described by the Lorentz-Drude model [44]:

$$\varepsilon = \varepsilon_{\infty}\left(1 - \frac{\omega_{\pi}^2}{\omega^2 + j\omega\Gamma}\right) \tag{1}$$

where ω is the angular frequency, ε_{∞} is the infinitive permittivity, Γ is the damping factor and ω_p is so-called as the plasma frequency that is defined by:

$$\omega_p = \sqrt{\frac{Ne^2}{\varepsilon_0 \varepsilon_{\infty} m^*}} \tag{2}$$

where e=1.6×10^{-19} C is the elementary charge of electron, ε_0 = 8.8541878128×10^{-12} F·m^{-1} is the vacuum permittivity, m^* is the electron effective mass, and N is the bulk free carrier concentration. Drude parameters are determined as: ε_{∞} = 3.9, Γ = 1.8 × 1014 rad/s and m^* = 0.35m_e , m_e is the free electron mass [44].

The resistivity ρ caused by ITO-based thin film can be attained as follows [44]:

$$\rho = \frac{\Gamma m^*}{Ne^2} \tag{3}$$

At a low-doped concentration (N = 10^{19} cm^{-3}) ITO supplies both characteristics of high-transparency ($\varepsilon'' \approx 0$) and high-resistivity. When the concentration is lower this level, ITO acts as a Mott insulator and becomes no longer conducting [38]. Otherwise, the light-matter interaction is considerably enhanced closely to the ENZ regime (N = 6.5 × 10^{20} cm^{-3}), where $\varepsilon' = 0$, $\varepsilon'' > 0$ and $|\varepsilon|$ achieves its minimum value ($|\varepsilon|$ = 0.57). As a result, optical losses may be drastically increased and thus, the transparency condition may be lost. However, when the lower-doped ITO, the resistivity becomes quite high leading the response time for switching larger. This can limit the promising potential for ultrafast applications. Therefore, in this paper, a free carrier concentration level of N=3 × 10^{20} cm^{-3} is chosen. Fig. 1 exhibits the permittivity parameters of (n, κ) of ITO as a function of the

wavelength when the free carrier concentration of N is 3×10^{20} cm^{-3}. At this value of the free carrier concentration, substituting into Exp. (1) we obtain $n + j\kappa = 1.27 + j0.125$. This value is also suitable to the experimental measurement results obtained from the sputtered films using the oxygen flow-rate and the post-deposition heat treatment process [37].

In this investigation, multiphysics and FEM numerical simulation tools of the Rsoft commercial simulation software are manipulated to characterize performance of ITO phase shifters with mesh sizes of $\Delta x = \Delta y = \Delta z = 5$ nm. The designated ITO phase shifters are applied for designing multimode selective devices. The proposed devices based on silicon photonic waveguides are implemented and optimized using the three-dimensional beam propagation method with ideal grid sizes.

3 Structure design and selection of the ITO phase shifter

The structural model of a ITO phase shifter is shown in Fig. 2(a), including a ITO thin film placed on the top of a silicon core waveguide. It is well-known that thermo-optic phase shifters are widely implemented in silicon photonics because of CMOS technology compatibility and the thermo-optic coefficient is sizeable with the bulk silicon crystal. When propagating the light field through the thermal phase shifter, under the impact of the heat flow that caused from the ITO heater in metallic state by a voltage source, the refractive index of waveguide Si can be tuned by changing the temperature of the phase shifter. This process leads a phase shift that can be determined by following relation [46]:

$$\Delta\Phi = \frac{2\pi L_{PS}}{\lambda_0}\frac{dn}{dT}\Delta T \tag{4}$$

where L_{PS} is the ITO heater length in the propagation direction, λ_0 is the operation wavelength, $\Delta T = T - T_0$ is the temperature change in the silicon waveguide core (T_0 = 300K is the room temperature), $\frac{dn}{dT}$ is the thermo-optic coefficient for silicon material, and $\frac{dn}{dT} = 1.84 \times 10^{-4}\, K^{-1}$ at the 1550-nm wavelength and at room temperature.

It is noted that the performance of the phase shifter does not depend on the heater length because the ITO heater length, L_{PS}, can be neglected since we combine both heat and optical phase shift equations. Hence, the same phase shift is induced for a given power consumption without considering the heater length [29]. In a thermo-optic phase shifter, the thermal conductivity reduction can improve the electric power consumption level by order of magnitude, but the switching time is usually worse to the same degree. Also, reducing the heater cross-section may lead to a rise in the current density and could melt the heater. Furthermore, the driving voltage will also be higher, and a more stringent alignment must be required if the heater is narrowed to the same order of the core waveguide width. Considering the thickness, fabricating the homogeneous and high-quality ITO thin-film structure becomes harder for thicknesses lower than 100 nm. As a result, in this study, three geometrical parameters, including the width W_{PS}, the length L_{PS}, and the thickness h_{PS} of the ITO heater, are set as 1 μm, 200 μm, and 100 nm, respectively.

Many TO phase shifters utilizing various materials such as Ti, ITO, Ag have been investigated in scientific reports. For a given metallic heater, the plasmonic effect can hybridize photonic mode propagating into silicon waveguide due to resonant condition at the metal-dielectric interface if the gap between metallic and silicon layers is small enough in several nanometer scales. This effect absorbs the photonic mode, thus limiting the propagation length of the optical field in the total inner reflection mechanism. To avoid the influence of the plasmonic effect, the gap of the silica layer sandwiched between the ITO and silicon layers is typically chosen as $h_{SiO_2} = 1$ μm [47]. Fig. 2(b) shows the propagation loss of the light when passing through the thermo-optic phase shifters, made from Ti and

ITO, depending on the gap h_{SiO_2} by using the multiphysics simulation tool. Simulated results show that the phase shifter made from Ti heater is more strongly influenced by the plasmonic effect than that of the ITO heater. When the gap is higher than 0.6 μm, the conductive losses due to the plasmonic effect are negligible for both Ti and ITO heaters. The distributions of the temperature rise (ΔT) and the index change (Δn) in the core layer are correspondingly shown to Fig. 2(c) and Fig. 2(d) by using the multiphysics tool when the ITO phase shifter is supplied by the electric power to achieve the tuned phase of π radian. In this work, the phase difference is changed from $-\pi/2$ to $\pi/2$ by the temperature rise (ΔT). As seen in Fig 2(e), the temperature rise changes from 0K to 120K to achieve the phase difference from 90 degrees to 270 degrees.

The power consumption of the phase shifter is estimated by the needed power to tune the desired phase of π radians (P_π). To evaluate the efficient function of a thermo-optical switch, we should consider the electric power consumption. For a given thermo-optic phase shifter, we require to obtain the optimal product of $P_\pi.\tau=H.\Delta T_\pi$ during the switching operation process. Here, H stands for the heat capacity, ΔT_π is the changing temperature from a cold state to a hot state to attain the expected phase shift of π, and τ is the switching time relating to the phase shifter temporal response and the cut-off frequency $f_{cut\text{-}off}$ [48]. The switching power consumption is estimated by using a modified two-dimensional treatment of heat flow on the lateral spreading:

The switching electric consumption power is determined by the following equation utilizing a modified two-dimensional treatment of the heat flow on the lateral spreading [49]:

$$P_\pi = \frac{\lambda \kappa_{SiO_2} \left(\frac{W_{PS}}{h_{SiO_2}} + 0.88 \right)}{\left| \frac{dn}{dT} \right|_{Si}} \tag{5}$$

where κ_{SiO_2} =1.4 W/(m.K) is the thermal conductivity of SiO_2, λ is the operation wavelength, and W_{PS} is the width of the ITO heater on the lateral direction.

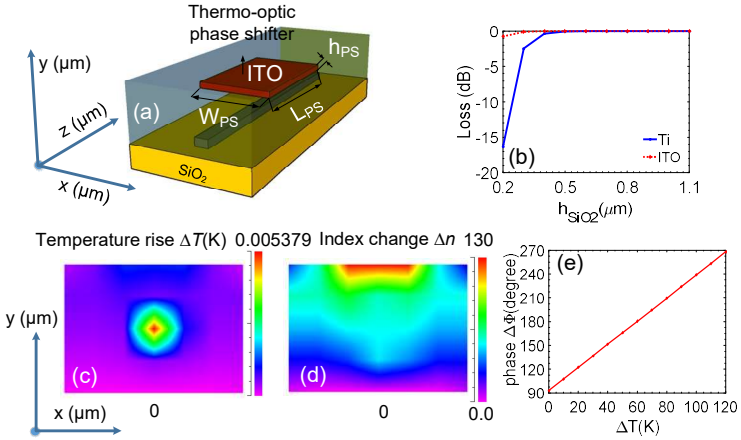

Fig. 2. Thermo-optic phase shifter based on ITO: **(a)** the structural diagram of a ITO phase shifter, **(b)** the simulated loss of Ti and ITO-based phase shifters depending on the silica gap between the silicon core layer and the microheater, **(c)** the temperature rise distribution on the ITO phase shifter simulated by using the multiphysics tool, **(d)** the index change distribution on the ITO phase shifter simulated by the multiphysics tool, and **(e)** the phase shift depending on the temperature change.

The switching time can be considered as a consequence of the required response time of the heat flow propagation from the micro-heater to the silicon core layer along the active length of the ITO phase shifter, which relates to the consumption power by the formula [26],, [48]:

$$\tau = \frac{\pi\lambda\rho_{SiO_2}C_{SiO_2}A}{eP_\pi\left|\frac{dn}{dT}\right|_{Si}} \quad (6)$$

where ρ_{SiO_2} =2.203 g/cm³ is density of silica, C_{SiO_2} =0.703 J/(g.K) is specific heat capacity of silica, $A = (2L_{th} + W_{PS})(h_{Si} + h_{SiO_2})$ is the effectively heated cross-section area relating to geometry parameters of the ITO phase shifter, h_{Si} = 220 nm is the thickness of the silicon core, $e \approx 2.7182818$ is the natural logarithm constant. L_{th} is the thermal diffusion length measured by taking the distance where the maximum temperature laterally decreased at $1/e^2$ away from the silicon waveguide.

The electric power consumption and the switching time are crucial parameters depending on geometrical structures such as the gap h_{SiO_2} and the width W_{PS} of the ITO heater, plotted in Fig. 3. Figs. 3(a,b) show the power consumption (P_π) and the switching time (τ) of the designated ITO phase shifter as functions of the width W_{PS} when the silica gap h_{SiO_2} is kept as 1 μm. The electric power consumed to reach the needed phase increases when the gap h_{SiO_2} increases. Therefore, in order to minimize the consumed power, the width W_{PS} is chosen as 1 μm which still attains the short switching time about 7 μs for the shifted phase of π radians. Also, when the width W_{PS} is fixed by 1 μm, the dependence of the power consumption (P_Φ) and the switching time (τ_Φ) on the gap h_{SiO_2} for several values of the phase shift Φ (π/2, π, 3π/2) are exhibited corresponding to Fig. 3(c,d), respectively. As a rule, the power consumption is an increasing function versus the gap. However, after reaching the highest point at the gap of h_{SiO_2} = 0.7um, the switching time decreases when the gap increases further. To achieve the phase difference of π/2, π, 3π/2, the electric power consumptions are corresponding to 9.85 mW, 17.83 mW, and 25.69 mW, and the time responses are corresponding to 6.53 μs, 7.2 μs, and 7.51 μs at the selected gap of h_{SiO_2} = 1 μm, respectively. All power consumption and switching time levels for the TO tuning phase are about some tens of milli-Watts and several microseconds, respectively, which are acceptable in the integrated photonic devices.

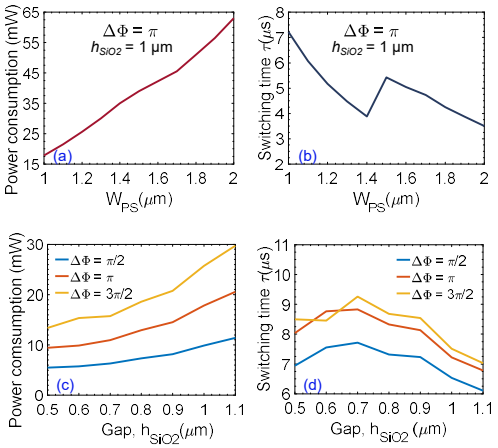

Fig. 3. ITO phase shifter characterizations: **(a, b)** the electric power consumption and the switching time as functions of the ITO microheater width when fixing the silica gap to reach the phase shift of π (radians), and **(c,d)** the electric power consumption and the switching time within the dependence on the silica gap at the ITO heater width of 1 μm for different shifted phase angles (π/2, π, 3π/2).

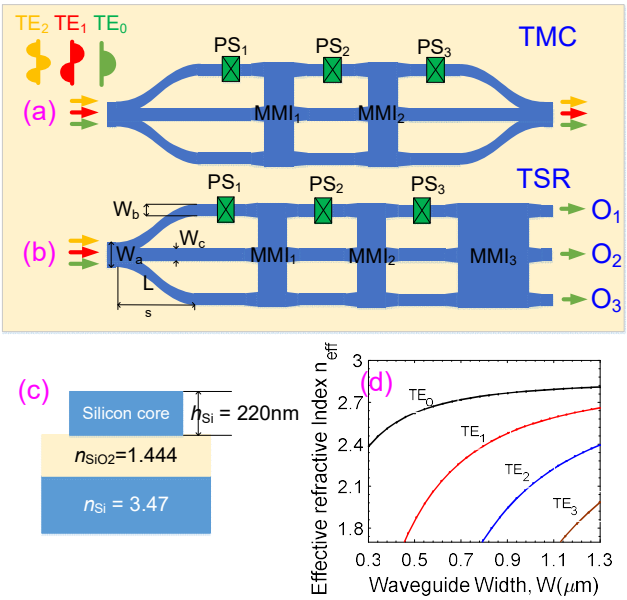

Fig. 4. A co-design of the multimode converter and the multimode selective router using ITO phase shifters based on silicon photonic waveguides: **(a, b)** top-view structural diagrams of a three-mode converter and a three-mode selective router, **(c)** the side-view of designated silicon photonic structures, and **(d)** the mode profile characterized by the effective refractive index on according to the input waveguide width solved by the mode solver tool of the Rsoft commercial software.

4. Applications of the ITO phase shifter in optical mode selective devices

For a given MDM system, a mode converter undertaking the mode order transforming mission and a multimode selective router exploiting the mode routing function play an indispensable role for a flexible mode division processing system. In this study, the schematic of a three-mode converter (TMC) and a three-mode selective router (TSR) are sketched correspondingly to Fig. 4(a) and Fig. 4(b), respectively. Both devices are constructed from fundamental elements composing of 3×3 multimode interference (MMI) couplers, symmetric Ψ-junction couplers, and ITO thermo-optic phase shifters. The proposed devices are designed and simulated by using channel structural waveguides based on the SOI material platform with the 220nm-silicon thickness and a cladding layer covered by the silica layer (SiO_2). On the top structure, an ITO thin-film layer, which structural parameters have been initially installed as mentioned above, is applied as TO phase shifters for realizing the mode selective functions, as seen in Fig. 4(c). The device is designed in the transverse electric (TE) polarization regime and the third telecom window with the central operation wavelength λ=1550 nm. The proposed device can be patterned from Deep Ultraviolet (DUV) photolithography with an illumination wavelength of 193-nm [50] and inductively coupled plasma (ICP) etching processes [51]. The ITO thin film can be easily formed with excellent quality via various deposition methods such as atomic layer deposition [52], pulsed layer deposition [53].

4.1. Symmetric Ψ-junction

A symmetric Ψ-junction, which acts as a mode decomposer (MDC), is specially designed to convert higher order-modes into fundamental mode. Following the mode-sorting principle suggested by D. Love et al. [54], if the effective index of the input is matched with the effective index of the fundamental mode in the output, the fundamental mode exists in these outputs. It is well-known that the effective index of the fundamental mode is the highest compared to all modes. Therefore, the larger waveguide has a higher effective index than the smaller waveguides. In this design, the outer waveguide width (W_b) of the MDC structure is narrower than the inner output waveguide width (W_c). Hence, the fundamental mode TE_0 will connect to the inner waveguide, and two higher-mode are

converted to two TE_0 mode components at two outer arms with equal amplitudes. However, two phases of two outer arms are out of phase when the input mode is TE_1. In contrast, two phases of two outputs are in phase when the input mode is TE_2. We apply the numerical simulation technique based on the three-dimensional beam propagation method (3D-BPM) to solve effective indexes of three lowest-order TE modes, plotted in Fig. 4(d). As a rule, we choose the input width of the MDC structure equally to W_a = 1.3 μm to support three guided modes, including TE_0, TE_1, TE_2. Two sinusoidal bending waveguides have the length L_s= 120 um and the width W_b = 0.5 μm. A straight waveguide in the middle is chosen W_c = 0.6 μm that only supports TE_0 mode. Fig. 5(a, b, c) show the results of decomposed mode components for both TE_0, TE_1, and TE_2 input modes when coupling to the MDC input. In MDC, the fundamental mode is propagated to the straight waveguide in the middle output waveguide of the Ψ-junction junction. Meanwhile, the first and the second-order mode is coupled to the outer arms at the output. Fig. 5 (d, e, f) illustrate wavelength responses of transmission curves corresponding to injected modes of TE_0, TE_1, TE_2, respectively. The simulated results show that, in all cases, transmission losses are smaller than 0,5 dB in broadband of 100-nm wavelength, and crosstalk is always lower than -25 dB for the undesired output ports.

4.2. 3×3 multimode interference couplers

Three kinds of 3×3 MMI couplers are used in these designs (so-called as MMI_1, MMI_2, and MMI_3 couplers). The width of multimode interferences is designed ideally to W_{MMI} = 6.8 μm. The length of MMI_1, MMI_2, and MMI_3 couplers correspond to L_{MMI_1}, L_{MMI_2}, L_{MMI_3}, respectively. Three input ports of three kinds of mentioned MMI couplers are placed at specific positions of $-W_{MMI}/3$, 0, $W_{MMI}/3$ along the x-coordinate, respectively. Noted that the symmetrical line goes through the central line of multimode structures. MMI_1 and MMI_2 couplers are ideal structures, which are 3×3 MMI couplers with their lengths $L_{MMI_1} = L_{MMI_2} = 3L_\pi/8$. While MMI_3 is a 3×3 MMI coupler that its length is defined as $L_{MMI_3} = 3L_\pi/2$ for exploiting the function of a 3 dB-coupler. Herein, L_π is a specific length of MMI coupler, so-called as the half-beat length, which is determined by the following equation [55]:

$$L_\pi = \frac{4 n_e W_e^2}{3\lambda} \tag{7}$$

where $W_e = W_{MMI} + \frac{\pi}{\lambda}\left(n_e^2 - n_c^2\right)^{-1/2}$ (for TE polarization mode)

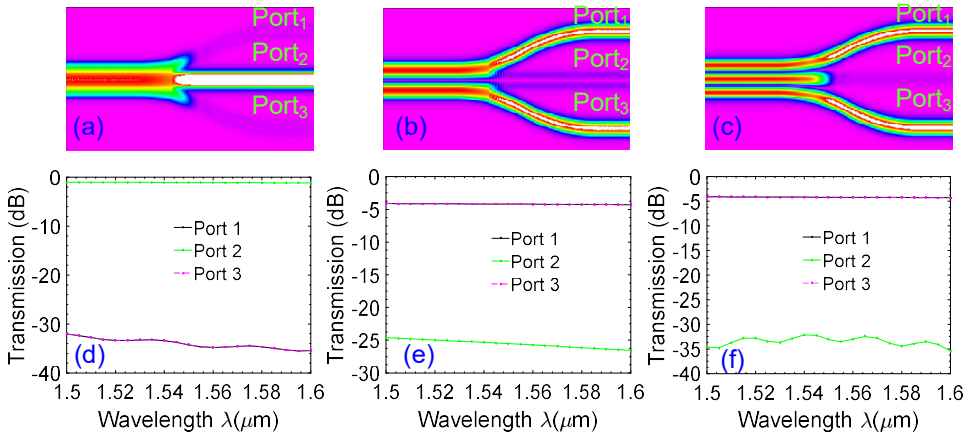

Fig. 5. The operating principle of the mode decomposer based on a symmetric Ψ-junction: **(a, b, c)** electric field patterns of the mode propagation corresponding to TE_0, TE_1, and TE_2 mode, respectively, **(d-f)** transmission spectral responses at output ports following the input modes of TE_0, TE_1, and TE_2 mode, respectively.

Tab. 1. Geometrical parameters of the proposed multimode selective devices.

Parameter	Value	Parameter	Value

L_{MMI_1}	44 μm	H_{PS}	100 nm
L_{MMI_2}	44 μm	W_{PS}	1 μm
L_{MMI_3}	176 μm	L_{PS}	120 μm
W_{MMI_1}	6.8 μm	W_a	1.3 μm
W_{MMI_2}	6.8 μm	W_b	0.5 μm
W_{MMI_3}	6.8 μm	W_c	0.6 μm
L_{PS}	200 μm	h_{SiO_2}	1 μm

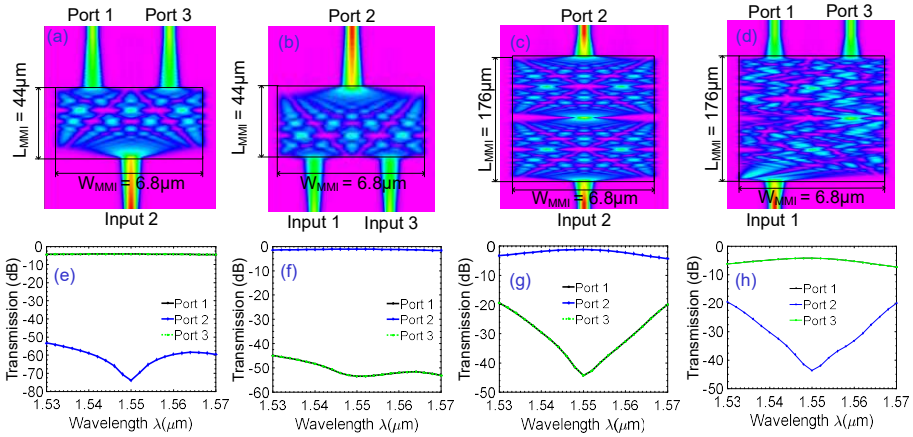

Fig. 6. Simulated operations of different 3×3 multimode interference couplers: **(a)** optical power splitting operation for MMI_1 and MMI_2 couplers when injecting the optical field at the central port, **(b)** optical power combining operation for MMI1 and MMI2 couplers at the central ports when injecting two in-phase optical fields at two outer arms, (**c)** the self-imaging process when injecting the optical field at the central input waveguide of the MMI_3 coupler,(d) the operating principle as a 3-dB coupler for two outer arms of the MMI_3 coupler, and **(e-h)** simulated spectral behaviors of different 3×3 MMI couplers corresponding to cases of **(a-d)**, respectively.

In which, n_e is the effective refractive index, n_c is the refractive index of the cladding layer, and λ is the operation wavelength of the device. Following the general interference (GI) principle, the self-imaging is periodically reproduced along the propagation direction of the z-coordinate. Fig. 6(a, b) present the simulated electric field patterns for MMI_1 and MMI_2 couplers, and Fig. 6(c, d) exhibit the simulated fields for the MMI_3 coupler when their lengths are optimized to attain the highest transmissions. For MMI_1 and MMI_2 couplers, the input light is injected to input 2 of the MMI1 coupler, the crosstalk is lower than -50 dB, and fluctuation of propagation loss is lower than 0.3 dB in the 40-nm wavelength response. When two input lights are coupled to input 1 and input 3 of MMI_1 and MMI_2 couplers, the power transmission at each desired output port is smaller than -1 dB, and the crosstalk at port 1 and port 3 are less than -45 dB in the wide band of 40-nm, as seen in Fig. 6(e, f). Also, for the MMI_3 coupler, one can see that a low transmission loss level of -1 dB is numerically measured with -44 dB of crosstalk at the wavelength of 1550 nm when the light field is injected into its central input port, as shown in Fig. 6(g). Also, the optical transmission spectrum of the MMI_3 coupler when guiding the light fields into its input 1, which plays the role of the 3-dB coupler, is illustrated in Fig. 6(h). It is seen that the desired powers at 1550 nm are about -4 dB while crosstalk is about -44 dB. In this work, all parameters optimized by simulation are listed in Tab. 1.

The transfer matrices of MMI_1 and MMI_2 couplers when injecting optical fields placed at specific positions above are deduced from Soldano et al. [55] by:

$$M = \begin{pmatrix} \frac{1}{2}e^{j\frac{\pi}{2}} & \frac{1}{\sqrt{2}} & \frac{1}{2}e^{j\frac{2\pi}{3}} \\ \frac{1}{\sqrt{2}} & 0 & \frac{1}{\sqrt{2}} \\ \frac{1}{2}e^{j\frac{2\pi}{3}} & \frac{1}{\sqrt{2}} & \frac{1}{2}e^{j\frac{\pi}{2}} \end{pmatrix} \tag{8}$$

Also, the transfer matrix of the MMI$_3$ coupler when access waveguides are placed at specific positions above is:

$$N = \begin{pmatrix} \frac{1}{\sqrt{2}} & 0 & \frac{1}{2}e^{j\frac{\pi}{2}} \\ 0 & 1 & 0 \\ \frac{1}{2}e^{j\frac{\pi}{2}} & 0 & \frac{1}{\sqrt{2}} \end{pmatrix} \tag{9}$$

where φ, is the accumulative phase angle when passing through the MMI$_1$ and MMI$_2$ couplers, θ is the accumulative phase angle when travelling the MMI$_3$ coupler.

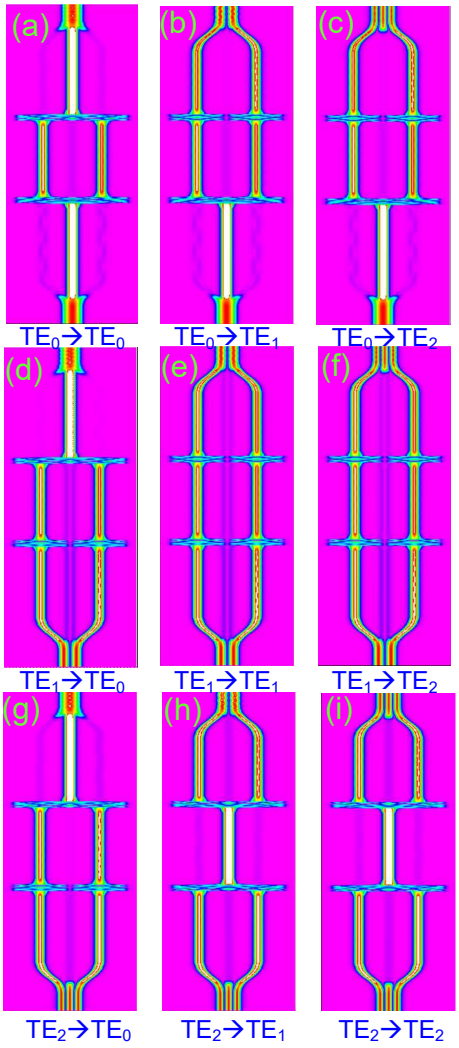

Fig. 7. Stimulated electric field patterns of the three-mode converter: **(a-c)** for the inputs of TE$_0$ modes, **(d-f)** for the inputs of TE$_1$ modes, and **(g-i)** for the inputs of TE$_2$ modes.

4.3. Operating principle and structural optimization of three-mode converter

This section introduces a proposal design for a three-mode converter (TMC) using the SOI material platform. The proposed TMC is made of two ideal 3×3 MMI couplers with the length of $3L_\pi/8$, two MDC elements, and three ITO thermo-optic phase shifters, as illustrated in Fig. 4(a). We analyze the operating principle of TMC when injecting three guided modes. First, the TE_0 mode is injected into the input port of MDC. This mode is propagated to the middle input port of MMI_1. The optical signal is divided into two outer outputs of MMI_1 with in-phase and in-amplitude. According to the transfer matrix described in Exp. (8), the signal is combined to the middle output port of MMI_2 and straight to the device output with the TE0 mode. If we tune the phase difference of $\Delta\Phi_2 = \pi$ radians, two lightwaves will be straightforwardly directed to two outer arms of MDC. At one of two outer arms of MDC, we put the phase shifter PS_3. If the phase of $\Delta\Phi_3 = 0$, they will be reformed to TE_1 at the end of the device's output. If the phase of $\Delta\Phi_3 = \pi$, two signals are combined and exchanged TE_0 to TE_2 in the output port.

Next, we assume that the TE_1 mode is coupled to the input of MDC. This mode will be divided into two curved waveguides of MDC with ideal magnitude and the opposite phase. Then, they propagated through the MMI_2 coupler before reaching the MMI_3 coupler if $\Delta\Phi_1 = 0$. The second MDC will combine and exchange to the TE_1 mode at this device output. Considering other cases, when the phase shifter PS_2 is changed a phase $\Delta\Phi_2 = \pi$, two optical signals are combined to the central output port of the MMI_2 coupler, and then this field will pass through to the TMC output with TE_0 mode. To convert the TE_1 mode becoming TE_2 mode, we need to tune the phase shift of $\Delta\Phi_3 = \pi$ while two remaining phase shifters are not operated because two fundamental modes in two output of MMI_2 will be transformed to TE_2 mode at the end of the stage.

Finally, we investigate when TE_2 mode is the input mode of MDC. After propagating into the input of MDC, two fundamental modes will exist in the two outer ports of MDC with in-amplitude and in-phase. Therefore, they are combined at the central output port of the MMI1 coupler and separated into two optical signals after propagating through MMI2 to connect two curved arms of MDC at the final stage. Naturally, the TE_2 mode will be originally reproduced into TMC without affecting phase shifters. To convert the TE_2 mode to the TE_0 mode, we need to change the phase shifts as $\Delta\Phi_1 = \pi$ and $\Delta\Phi_2 = \pi$ while keeping the original state of PS_3. Also, to exchange the TE_2 mode to the TE_1 mode, we only implement the phase change of $\Delta\Phi_3 = \pi$ without adjusting two remaining phase shifters. Fig. 7(a-i) show the simulated electric field patterns for nine possible cases of mode conversion states by using the 3D-BPM simulation method. It can be seen that all cases are demonstrated exactly as theoretically analyzed.

4.4. Operating principle and structural optimization of three-mode selective router

This section proposes a novel design of a three-mode selective router (TSR) based on three MMI couplers, an MDC, and three ITO thermo-optic phase shifters, expressed in Fig. 4(b). The Ψ-junction-based MDC is placed at the TSR input port for decomposing the guided modes to fundamental modes. Two ideal 3×3 MMI couplers, namely MMI_1, MMI_2 with the length of $3L_\pi/8$, are concatenated later. At the last stage, a 3×3 MMI coupler, namely MMI_3 with a length of $3L_\pi/2$, is responsible for the mode routing mission.

Next, we analyze the working mechanism of three guided modes into the proposed router. First, in the case of input mode is TE_0. This mode is coupled to the central output port of the Ψ-junction coupler. It then is guided into the input port of the MMI1 coupler and is divided into two of its outer output arms with in-amplitude and in-phase according to the transfer matrix from Exp. (8) and Exp. (9). These optical paths are led to the MMI_2 coupler via the phase shifter of PS_2. If the phase difference $\Delta\Phi_2=0$, two optical signals will be straightforwardly directed to two outer arms of the MMI3 that one arm is traveled the phase shifter PS_3. The MMI_3 plays the role of a 3-dB coupler for two outer optical paths because the MMI3 coupler length is $3/2L_\pi$. Hence, if the phase shifter $\Delta\Phi_3$ is $\pi/2$, the MMI_3 coupler will combine two optical signals at the output port O_1. If the phase shifter $\Delta\Phi_3$ is $-\pi/2$, MMI_3 will combine two optical signals at the output port O_3. In another scenario, if the phase shift $\Delta\Phi_2$ is π, the combined optical signals will be focused on a unique signal

at the central input port of the MMI_3 coupler. That reason is due to the MMI_3 length as $3L_\pi/2=2\times3L_\pi/4$, thus following the symmetric interference rule, this optical field is reproduced at the central output port O_2 of the MMI_3 coupler.

Assume that the input mode at the stem of the Ψ-junction coupler is the TE_1 mode. It is decomposed into a pair of fundamental modes at two outward branches of the Ψ-junction coupler with the same magnitude and out of phase. If phase shift $\Delta\Phi_1$ is 0, these two signals will continue to be straightforwardly transmitted through the output arms of MMI_1. Depending on the phase shift status of the PS_2, optical signals are routed to different outputs. If $\Delta\Phi_2 = 0$, these two routes continue to pass through the MMI_2 coupler before reaching the MMI_3 coupler. At the last stage, if $\Delta\Phi_2 = \pi/2$, the optical signal is combined at the output O_1, and vice versa, if $\Delta\Phi_2 = -\pi/2$, the optical signal is switched to the output O_3. In order for TE1 mode to be switched to the output O_2, the phase shift action of PS_2 needs to be controlled so that $\Delta\Phi_2 = \pi$, then the two optical lines will be combined at the central output port of MMI_2 and directed to the output O_2 because of the symmetrical interference property of the MMI_3 coupler.

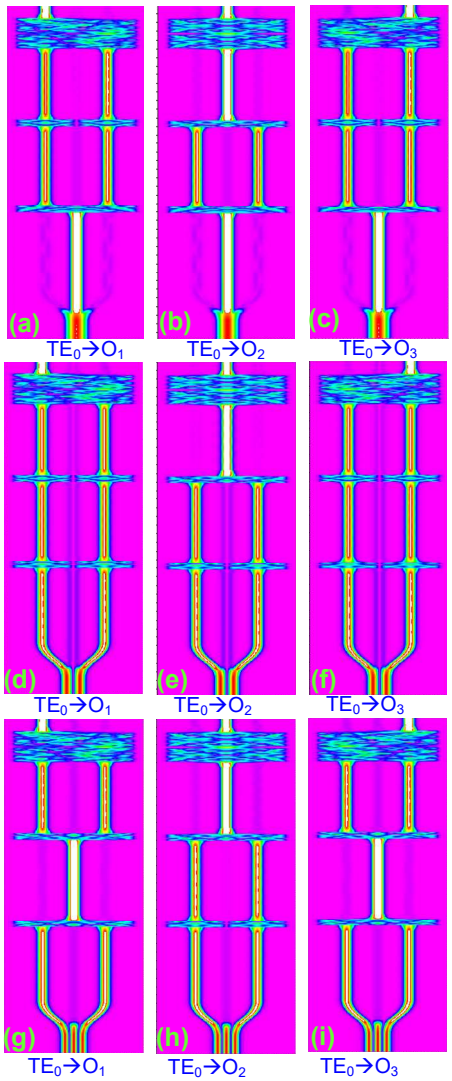

Fig. 8. Stimulated electric field patterns of the three-mode selective router: **(a-c)** for the inputs of TE_0 modes, **(d-f)** for the inputs of TE_1 modes, and **(g-i)** for the inputs of TE_2 modes.

Analogously, we also get the non-blocking activities of TE_2 mode. It means TE_2 mode can be optionally switched to the three outputs of the proposed router freely. We note that the non-invasive action between TE_1 and TE_2 modes is because mode TE_2 will be coupled with two output arms with the same amplitude but out of phase. Nine simulated electric field

distributions for independent mode selective states of the designated router when injecting three guided modes of TE_0, TE_1, and TE_2 are exhibited correspondingly to Fig. 8 (a-i), respectively. It is visible to see that all cases are exact to the theoretical analysis.

4.5. Characterization of the proposed mode converter and mode selective router and discussion

Optical losses when traveling through the designed ITO phase shifter were negligible in agreement with the simulation result. Likewise, the sidewall roughness losses could be trivial if a high-resolution photolithography process is applied to fabricate proposed devices. Therefore, in optical characterizations, insertion loss (I.L) caused by propagation and radiation losses and crosstalk (Cr.T) caused by undesirable optical sources are considered critical contributions for device's optical performances. Fig. 9(a, b, c) show the simulated spectrum of the TMC structure in a broadband of 100-nm wavelength for the 3-dB bandwidth with the suggested ITO phase shifters corresponding to input signals of TE_0, TE_1, TE_2, respectively. Whereas, Fig. 9(d-i) illustrate the simulated transmission spectrum for the TSR structure. As a result, 3-dB wavelength bandwidths of the I.L transmission in nine cases, which are measured from simulated data, show a high wavelength spectrum of 40-nm from 1530-1570 nm while assuring crosstalk always lower than -20 dB. Herein, we denote A, B, and C cases corresponding to the optical modes switched to the desired output ports of O_1, O_2, and O_3, respectively. Furthermore, in this work, the designated devices can be arranged in a compact footprint of 8 μm×2160 μm.

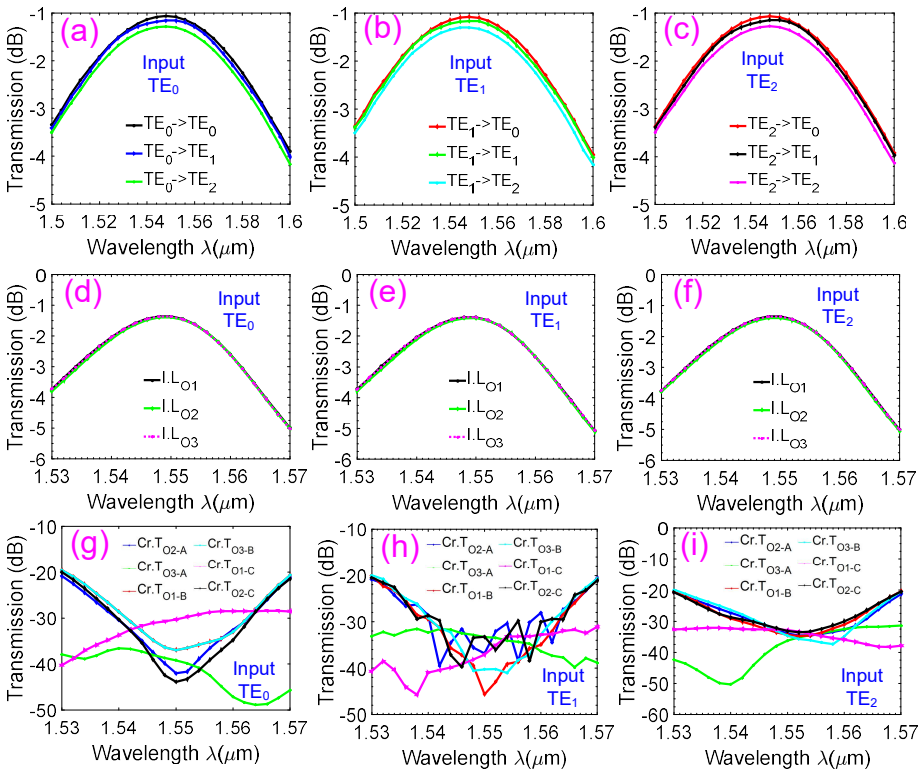

Fig. 9. Numerically stimulated wavelength spectrum responses of the TMC and TSR: (a, b, c) mode selective conversion efficiencies of the TMC structure according to input signals of TE_0, TE_1, TE_2, respectively, (d, e, f) insertion loss transmissions at output ports of the TSR structure according to input signals of TE_0, TE_1, TE_2, and (g, h, i) crosstalk transmission at output ports of the TSR structure according to input signals of TE_0, TE_1, TE_2, respectively.

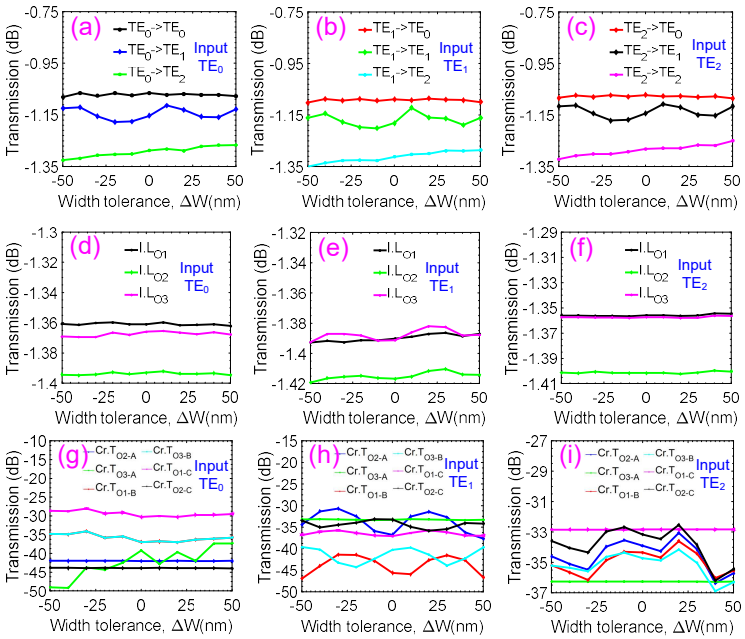

Fig. 10. Numerically stimulated width tolerances of the TMC and TSR: (a, b, c) mode selective conversion efficiencies of the TMC structure according to input signals of TE_0, TE_1, TE_2, respectively, (d, e, f) insertion loss transmissions at output ports of the TSR structure according to input signals of TE_0, TE_1, TE_2, and (g, h, i) crosstalk transmission at output ports of the TSR structure according to input signals of TE_0, TE_1, TE_2, respectively.

In integrated silicon photonics, the devices always suffer some errors from the manufacturing process that are caused from the resolution limit of the fabrication technology and the purity of supplied SOI wafer. Hence, the fabrication tolerances are necessary for photonic integrated circuits, especially for simulation-based designs. In Fig. 10 (a, b, c) are shown the slight variations of the I.L transmission not exceeded 0.02 dB in a large width tolerance of the input waveguide $\Delta W = \pm 50$ nm for the TMC structure. The I.L variation is also tiny for three guided modes in the TSR device, about 0.02 dB in ±50 nm width tolerance while keeping the Cr.T level lower than -28 dB for three guided modes, as seen in Fig. 10(d-i). Fig. 11(a-c) exhibit the I.L dependences on the length tolerance Δh of the silicon thickness for the TMC structure. Whereas, Fig. 11(d-i) depict the I.L and Cr.T transmissions for the TSR structure. It can be seen that I.L fluctuates slightly from -1.1 dB to -1.81 dB for TMC in a relatively large tolerance of Δh=±5 nm. Also, I.L fluctuates in a small gap from -1.4 dB to -2.3 dB, and Cr.T is not higher than -25 dB in a height tolerance of Δh=±5 nm. The current advanced fabrication technology, such as 193-nm photolithography, can obtain such tolerances.

5. Conclusions

In summary, we presented a co-design of compact and high bandwidth mode selective devices based on silicon-on-insulator waveguides, which can achieve multiple functions of a three-mode converter and a three-mode selective router by tuning the phase shift in low-loss ITO thermo-optic phase shifters. Simulation results have demonstrated the 3-dB bandwidth for the three-mode converter and three-mode selective router as much as 100-nm and 40-nm while preserving crosstalk under -25 dB, respectively. Besides, two designated devices also had relatively large fabrication tolerances corresponding to width and height tolerances of ±50 nm and ±5 nm, respectively. The proposed devices consumed a low power consumption not exceeded 90 mW and spent a short time below 8 μs in switching the operating states. Moreover, both two co-designs can be integrated into a compact footprint of 8 μm×2160 μm. Such excellent performances of the proposed structures make designed devices a promising potential for applications in high-speed mode division multiplexing systems and very large-scale photonic integrated circuits.

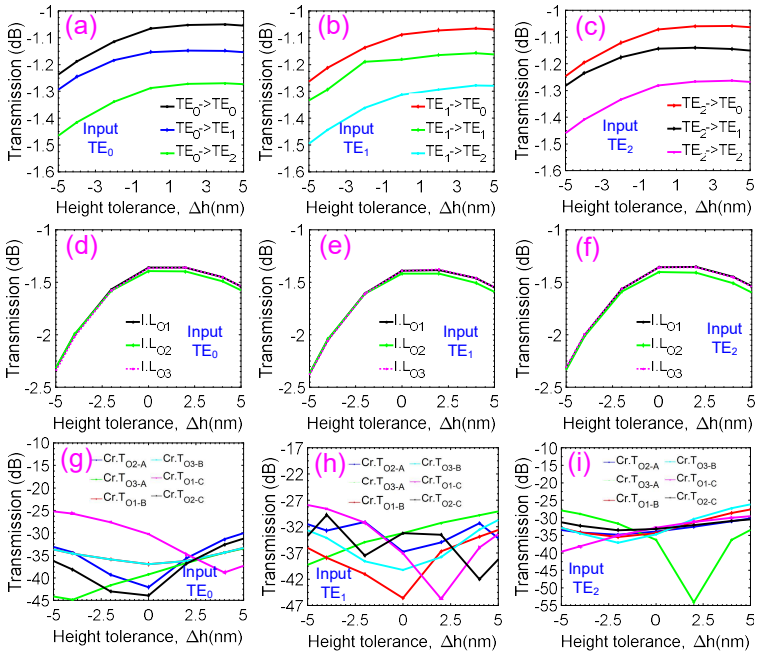

Fig. 11. Numerically stimulated height tolerances of the TMC and TSR: (a, b, c) mode selective conversion efficiencies of the TMC structure according to input signals of TE_0, TE_1, TE_2, respectively, (d, e, f) insertion loss transmissions at output ports of the TSR structure according to input signals of TE_0, TE_1, TE_2, and (g, h, i) crosstalk transmission at output ports of the TSR structure according to input signals of TE_0, TE_1, TE_2, respectively.

Author Contributions: Conceptualization, C.D.T., H.T.D., and D.N.T.H.; methodology, C.D.T.; software, H.T.D., D.N.T.H; validation, T.T.T.T., D.D.Q. and H.C.D.; formal analysis, T.T.T.T. and H.C.D.; investigation, C.D.T., D.N.T.H. and T.T.T.T.; resources, H.T.D., D.N.H.T, and D.D.Q.; data curation, D.H.T., D.N.H.T, and D.D.Q; writing—original draft preparation, H.T.D., D.N.T.H.; writing—review and editing, C.D.T.; visualization, D.H.T., H.C.D.; supervision, C.D.T.; project administration, C.D.T., H.C.D.; funding acquisition, D.H.T, D.N.T.H, T.T.T.T., and C.D.T. All authors have read and agreed to the published version of the manuscript.

Funding: This research was funded by Vingroup Innovation Foundation (VINIF), grant number VINIF.2019.DA12.

Acknowledgments: In this section, you can acknowledge any support given which is not covered by the author contribution or funding sections. This may include administrative and technical support, or donations in kind (e.g., materials used for experiments).

Conflicts of Interest: The authors declare no conflict of interest.

References

1. T. Morioka, Y. Awaji, R. Ryf, P. Winzer, D. Richardson, and F. Poletti, "Enhancing optical communications with brand new fibers," *IEEE Commun. Mag.* **50**, 31–42 (2012).
2. E. Granot and S. Sternklar, "Limitations to bit-rate and spatial capacity of an optical data transmission channel," J. Opt. A **4**, 2–4 (2002).
3. A. D. Ellis, J. Zhao, and D. Cotter, "Approaching the Non-Linear Shannon Limit," J. Light. Technol. **28**, 423–433 (2010).
4. K. Roberts, Q. Zhuge, I. Monga, S. Gareau, and C. Laperle, "Beyond 100 Gb/s: Capacity, flexibility, and network optimization [invited]," *J. Opt. Commun. Netw.* **9**, C12–C24 (2017).
5. X. Wang, F. Zhou, S. Yan, Y. Yu, J. Dong, and X. Zhang, "Broadband on-chip integrator based on silicon photonic phase-shifted Bragg grating," *Photonics Res.* **5**, 182 (2017).
6. A. M. Bratkovsky, J. B. Khurgin, E. Ponizovskaya, W. V. Sorin, and M. R. T. Tan, "Mode division multiplexed (MDM) waveguide link scheme with cascaded Y-junctions," *Opt. Commun.* **309**, 85–89 (2013).
7. D. Guo and T. Chu, "Silicon mode (de)multiplexers with parameters optimized using shortcuts to adiabaticity," *Opt. Express*

25, 9160 (2017).

8. D. Dai and M. Mao, "Mode converter based on an inverse taper for multimode silicon nanophotonic integrated circuits," *Opt. Express* **23**, 28376 (2015).
9. B. Stern, X. Zhu, C. P. Chen, L. D. Tzuang, J. Cardenas, K. Bergman, and M. Lipson, "On-chip mode-division multiplexing switch," *Optica* **2**, 530 (2015).
10. R. B. Priti, H. P. Bazargani, Y. Xiong, and O. Liboiron-Ladouceur, "Mode selecting switch using multimode interference for on-chip optical interconnects," *Opt. Lett.* **42**, 4131–4134 (2017).
11. X. Wang and K. S. Chiang, "Polarization-insensitive mode-independent thermo-optic switch based on symmetric waveguide directional coupler," *Opt. Express* **27**, 35385 (2019).
12. A. Masood, M. Pantouvaki, D. Goossens, G. Lepage, P. Verheyen, J. Van Campenhout, P. Absil, D. Van Thourhout, and W. Bogaerts, "Fabrication and characterization of CMOS-compatible integrated tungsten heaters for thermo-optic tuning in silicon photonics devices," *Opt. Mater. Express* **4**, 1383 (2014).
13. M. Takenaka, Y. Kim, J. Han, J. Kang, Y. Ikku, Y. Cheng, J. Park, M. Yoshida, S. Takashima, and S. Takagi, "Heterogeneous CMOS Photonics Based on SiGe/Ge and III-V Semiconductors Integrated on Si Platform," *IEEE J. Sel. Top. Quantum Electron.* **23**, (2017).
14. D. Inoue, T. Ichikawa, A. Kawasaki, and T. Yamashita, "Silicon optical modulator using a low-loss phase shifter based on a multimode interference waveguide," *Micromachines* **10**, (2019).
15. S. A. Miller, Y.-C. Chang, C. T. Phare, M. C. Shin, M. Zadka, S. P. Roberts, B. Stern, X. Ji, A. Mohanty, O. A. Jimenez Gordillo, U. D. Dave, and M. Lipson, "Large-scale optical phased array using a low-power multi-pass silicon photonic platform," *Optica* **7**, 3 (2020).
16. J. Sun, E. Timurdogan, A. Yaacobi, E. S. Hosseini, and M. R. Watts, "Large-scale nanophotonic phased array," *Nature* **493**, 195–199 (2013).
17. J. Sun, E. Timurdogan, A. Yaacobi, Z. Su, E. S. Hosseini, D. B. Cole, and M. R. Watts, "Large-scale silicon photonic circuits for optical phased arrays," *IEEE J. Sel. Top. Quantum Electron.* **20**, (2014).
18. R. Amin, R. Maiti, J. K. George, X. Ma, Z. Ma, H. Dalir, M. Miscuglio, and V. J. Sorger, "A Lateral MOS-Capacitor-Enabled ITO Mach-Zehnder Modulator for Beam Steering," *J. Light. Technol.* **38**, 282–290 (2020).
19. D. Dai, "Silicon Nanophotonic Integrated Devices for On-Chip Multiplexing and Switching," *J. Light. Technol.* **35**, 572–587 (2017).
20. F. Testa, S. Tondini, F. Gambini, P. Velha, A. Bianchi, C. Kopp, M. Hofbauer, C. L. Manganelli, N. Zecevic, S. Faralli, G. Pares, R. Enne, A. Serrano, B. Goll, G. Fontana, A. Chalyan, J. M. Lee, P. Pintus, G. Chiaretti, H. Zimmermann, L. Pavesi, C. J. Oton, and S. Stracca, "Integrated reconfigurable silicon photonics switch matrix in IRIS project: Technological achievements and experimental results," *J. Light. Technol.* **37**, 345–355 (2019).
21. R. Amin, R. Maiti, Y. Gui, C. Suer, M. Miscuglio, E. Heidari, J. B. Khurgin, R. T. Chen, H. Dalir, and V. J. Sorger, "Heterogeneously integrated ITO plasmonic Mach–Zehnder interferometric modulator on SOI," *Sci. Rep.* **11**, 1–12 (2021).
22. J. Kim, S. Aghaeimeibodi, J. Carolan, D. Englund, and E. Waks, "Hybrid integration methods for on-chip quantum photonics," *Optica* **7**, 291–308 (2020).
23. F. Meinert, C. Hölzl, M. A. Nebioglu, A. D'Arnese, P. Karl, M. Dressel, and M. Scheffler, "Indium tin oxide films meet circular Rydberg atoms: Prospects for novel quantum simulation schemes," *Phys. Rev. Res.* **023192**, 1–7 (2020).
24. Y. Shen, N. C. Harris, S. Skirlo, M. Prabhu, T. Baehr-Jones, M. Hochberg, X. Sun, S. Zhao, H. Larochelle, D. Englund, and S. Marin, "Deep learning with coherent nanophotonic circuits," *Nat. Photonics* **11**, 441–446 (2017).
25. A. Forouzmand and H. Mosallaei, "Real-Time Controllable and Multifunctional Metasurfaces Utilizing Indium Tin Oxide Materials: A Phased Array Perspective," *IEEE Trans. Nanotechnol.* **16**, 296–306 (2017).
26. V. M. N. Passaro, F. Magno, and A. V. Tsarev, "Investigation of thermo-optic effect and multi-reflector tunable filter/multiplexer in SOI waveguides," *Opt. Express* **13**, 3429 (2005).

27. Q. Huang, K. S. Chiang, and W. Jin, "Thermo-optically controlled vertical waveguide directional couplers for mode-selective switching," *IEEE Photonics J.* **10**, 1–14 (2018).
28. P. Sun and R. M. Reano, "Submilliwatt thermo-optic switches using free- standing silicon-on-insulator strip waveguides," *Opt. Express* **18**, 1315–1320 (2010).
29. M. Jacques, A. Samani, E. El-Fiky, D. Patel, Z. Xing, and D. V. Plant, "Optimization of thermo-optic phase-shifter design and mitigation of thermal crosstalk on the SOI platform," *Opt. Express* **27**, 10456 (2019).
30. A. H. Atabaki, E. S. Hosseini, A. A. Eftekhar, S. Yegnanarayanan, and A. Adibi, "Optimization of metallic micro-heaters for reconfigurable silicon photonics," *Opt. Express* **18**, 18312–18323 (2010).
31. L. Yu, Y. Yin, Y. Shi, D. Dai, and S. He, "Thermally tunable silicon photonic microdisk resonator with transparent graphene nanoheaters," *Optica* **3**, 159 (2016).
32. Z. Xu, C. Qiu, Y. Yang, Q. Zhu, X. Jiang, Y. Zhang, W. Gao, and Y. Su, "Ultra-compact tunable silicon nanobeam cavity with an energy-efficient graphene micro-heater," *Opt. Express* **25**, 19479 (2017).
33. C. Ye, S. Khan, Z. R. Li, E. Simsek, and S. Member, "λ -Size ITO and Graphene-Based Electro-Optic," *IEEE J. Sel. Top. Quantum Electron.* **20**, 3400310 (2014).
34. Z. Ma, Z. Li, K. Liu, C. Ye, and V. J. Sorger, "Indium-Tin-Oxide for High-performance Electro-optic Modulation," *Nanophotonics* **4**, 198–213 (2015).
35. R. Amin, C. Suer, Z. Ma, I. Sarpkaya, J. B. Khurgin, R. Agarwal, and V. J. Sorger, "Active material, optical mode and cavity impact on nanoscale electro-optic modulation performance," *Nanophotonics* **7**, 455–472 (2017).
36. G. Sinatkas and E. E. Kriezis, "Silicon-Photonic Electro-Optic Phase Modulators Integrating Transparent Conducting Oxides," *IEEE J. Quantum Electron.* **54**, 1 (2018).
37. Y. Gui, M. Miscuglio, Z. Ma, M. H. Tahersima, S. Sun, R. Amin, H. Dalir, and V. J. Sorger, "Towards integrated metatronics: a holistic approach on precise optical and electrical properties of Indium Tin Oxide," *Sci. Rep.* **9**, 1–10 (2019).
38. L. Caspani, R. P. M. Kaipurath, M. Clerici, M. Ferrera, T. Roger, J. Kim, N. Kinsey, M. Pietrzyk, A. Di Falco, V. M. Shalaev, A. Boltasseva, and D. Faccio, "Enhanced Nonlinear Refractive Index in ϵ -Near-Zero Materials," *Phys. Rev. Lett.* **116**, 1–5 (2016).
39. A. D. Neira, G. A. Wurtz, and A. V. Zayats, "All-optical switching in silicon photonic waveguides with an epsilon-near-zero resonant cavity [Invited]," *Photonics Res.* **6**, B1 (2018).
40. M. Z. Alam, I. De Leon, and R. W. Boyd, "Large optical nonlinearity of indium tin oxide in its epsilon-near-zero region," *Science* (80-.). (2016).
41. P. Guo, R. D. Schaller, L. E. Ocola, B. T. Diroll, J. B. Ketterson, and R. P. H. Chang, "Large optical nonlinearity of ITO nanorods for sub-picosecond all-optical modulation of the full-visible spectrum," *Nat. Commun.* **7**, 1–10 (2016).
42. S. Rajput, V. Kaushik, S. Jain, and M. Kumar, "Slow light enhanced phase shifter based on low-loss silicon-ITO hollow waveguide," *IEEE Photonics J.* **11**, 1–8 (2019).
43. R. Amin, R. Maiti, C. Carfano, Z. Ma, M. H. Tahersima, Y. Lilach, D. Ratnayake, H. Dalir, and V. J. Sorger, "0.52 v mm ITO-based Mach-Zehnder modulator in silicon photonics," *APL Photonics* **3**, 0–11 (2018).
44. J. Parra, J. Hurtado, A. Griol, and P. Sanchis, "Ultra-low loss hybrid ITO/Si thermo-optic phase shifter with optimized power consumption," *Opt. Express* **28**, 9393 (2020).
45. D. Chen, X. Xiao, L. Wang, Y. Yu, W. Liu, and Q. Yang, "Low-loss and fabrication tolerant silicon mode-order converters based on novel compact tapers," *Opt. Express* **23**, (2015).
46. M. Jacques, A. Samani, E. El-Fiky, D. Patel, Z. Xing, and D. V Plant, "Optimization of thermo-optic phase-shifter design and mitigation of thermal crosstalk on the SOI platform," *Opt. Express* **27**, 10456–10471 (2019).
47. R. B. Priti and O. Liboiron-Ladouceur, "Reconfigurable and Scalable Multimode Silicon Photonics Switch for Energy Efficient Mode-division-multiplexing Systems," *J. Light. Technol.* **37**, 3851–3860 (2019).
48. R. L. Espinola, M. C. Tsai, J. T. Yardley, and R. M. Osgood, "Fast and low-power thermooptic switch on thin silicon-on-insulator," *IEEE Photonics Technol. Lett.* **15**, 1366–1368 (2003).

49. K. Liu, C. Zhang, S. Mu, S. Wang, and V. J. Sorger, "Two-dimensional design and analysis of trench-coupler based Silicon Mach-Zehnder thermo-optic switch," *Opt. Express* **24**, 15845 (2016).
50. M. Totzeck, W. Ulrich, A. Göhnermeier, and W. Kaiser, "Semiconductor fabrication: Pushing deep ultraviolet lithography to its limits," *Nat. Photonics* **1**, 629–631 (2007).
51. M. Nedeljkovic, A. Z. Khokhar, Y. Hu, X. Chen, J. S. Penades, S. Stankovic, H. M. H. Chong, D. J. Thomson, F. Y. Gardes, G. T. Reed, and G. Z. Mashanovich, "Silicon photonic devices and platforms for the mid-infrared," *Opt. Mater. Express* **3**, 1205 (2013).
52. R. W. Johnson, A. Hultqvist, and S. F. Bent, "A brief review of atomic layer deposition: From fundamentals to applications," *Mater. Today* **17**, 236–246 (2014).
53. J. Schou, "Physical aspects of the pulsed laser deposition technique: The stoichiometric transfer of material from target to film," *Appl. Surf. Sci.* **255**, 5191–5198 (2009).
54. N. Riesen and J. D. Love, "Design of mode-sorting asymmetric Y-junctions," *Appl. Opt.* **51**, 2778–2783 (2012).
55. L. B. Soldano and E. C. M. Pennings, "Optical Multi-Mode Interference Devices Based on Self-Imaging: Principles and Applications," *J. Light. Technol.* **13**, 615–627 (1995).